

Nanostructured micrometric-pore membranes for nanofiltration: Micrometric geometry may optimize performance, energy efficiency and operational lifetime

J.C. Verde,^{1, a)} N. Cotón,^{1, b)} and M.V. Ramallo^{1, c)}

*QMatterPhotonics Research Group, Department of Particle Physics,
University of Santiago de Compostela 15782, Spain^{d)}*

(*Electronic mail: mv.ramallo@usc.es)

Abstract:

Media and membranes composed of micrometric-diameter pores are well known in academia and industry to be capable of efficacious nanofiltration of fluids once the pore inner surfaces are coated with nanostructures. Given the large mismatch between the two very different scales of these hybrid systems, it could be expected that trapping of nanoimpurities would almost entirely depend on the characteristics of the nanostructures. However, we show here that the micrometric-scale nominal geometry does have noticeable impact on the nanofiltration performance, on its evolution with time, and on the energy spent per trapped impurity. For that, we apply stochastic calculations customized to combine the cumulative probabilities of wall-impurity attraction and binding, supplemented with continuity equations as the fluid flows; this allows tracking the nanofiltration without a many-particle simulation, prohibitive in such multi-scale system. We focus on the influence of the micrometric nominal geometry over filtration features like logarithmic removal value LRV, operational lifetimes, energy balances, or spatial profiles of the trapped-impurity layer in the pore inner walls. Our results identify some pore geometries (*e.g.*, decreasing-conical and sinusoidal-corrugated) with about 4-fold larger initial nanofiltration performance and operational lifetime than simple cylinders of the same average diameter. The optimal geometry is also shown to depend on the LRV value acceptable for each specific application.

^{a)}In leave of absence

^{b)}Currently at Materials Physics Department, Complutense University of Madrid 28040, Spain

^{c)}Also at Institute of Materials iMATUS, University of Santiago de Compostela 15782, Spain

^{d)}<http://qmatterphotonics.usc.es>

I. INTRODUCTION

One of the most innovative and promising techniques for water filtration is the application of nanotechnology.^{1–5} Some examples of very interesting results achieved by research in the topic include, *e.g.*, the fabrication of new nanoenhanced membrane and media,^{6–22} or the development of theory and stochastic models^{23–33} customized to explain the behavior of novel filtrating elements and/or mechanisms. For example, in recent years both experimentalists and industry^{6–17} have become progressively interested in membranes that achieve nanofiltration by means of nanofunctionalization of the inner walls of pores with diameters in the micrometric range $\sim 0.2\text{--}2\ \mu\text{m}$. In these investigations^{6–17} it has been revealed the surprisingly good capability of these pores to filter out nanosized impurities from fluids, principally when the signs of the ζ -potentials of impurities and functionalized pore walls are opposite so that electrostatic effects enhance the filtration.^{6–17,23,24} This is in spite of such a relatively large diameter of the pores (note that for a pressure-driven flow passing through a cylindrical conduit with diameter $1\ \mu\text{m}$, only about 0.04% of the fluid will transit closer than 10 nm from the walls). A key practical advantage of these novel nano/micro hybrid-scale membranes is that they are not affected by the very large hydrodynamic resistance of pores of nanometric-scale diameters. Also their saturation capacity is much larger than for membranes of the same area but composed of nanometric-diameter pores. In fact, nanostructured micrometric pore membranes are currently commercialized for, *e.g.*, energy-efficient nanofiltration of drinking water, clinical virus sampling, COVID masks of reduced breathing effort, industrial effluents treatment, etc.^{6,9–12}

It is currently possible to custom-engineer the geometry profiles of micrometric-diameter pores of filtering membranes (see, *e.g.*, Refs. 34–38 for a description of different ad-hoc geometries and the experimental techniques used to obtain them). These feasible designs include, among others, tubular conduits with cylindrical shapes having different diameters,³⁴ corrugated tubes,³⁵ or pores with cone-like shapes.^{36–38} But to our knowledge such engineering has never been used with nanostructured micrometric pores.

To our knowledge no experimental or theoretical investigation seems to exist up to now of the influence over the nanofiltration of the nominal micrometric geometry of nanostructured micrometric pores, maybe because one could naïvely expect that due to the large mismatch between the two very different scales of these hybrid systems, the nanofiltration characteristics would almost

entirely depend on the characteristics of the nanostructures, and not on the micrometric geometry.

In this article we present a theoretical study of the influence of micrometric-scale nominal geometry in the nanofiltration characteristic of a single nanostructured micrometric pore, that reveals that micrometric geometry may in fact have considerable influence on various of the nanofiltration figures of merit, such as the logarithmic removal value LRV, the energy required for filtration, or the operational lifetimes. Our results should be directly applicable to membranes composed of such pores. They could be also useful for future investigations in three-dimensional porous media, where local tortuosity of the intensity and orientation of flow in each pore should be additionally considered. Also, investigating pores with different nominal geometries may also be relevant for random media, in which interconnections and throats between pores may be studied in terms of conduits with sinus-like corrugated shapes.^{39–42}

For our study, we will apply stochastic calculations custom-adapted to combine cumulative probabilities of wall-impurity attraction and binding, supplemented with continuity equations as the fluid flows. For the wall-impurity attraction and binding probabilities, we employ considerations adapted to the specific attraction produced by these electropositive (or negative) nanotextured walls over nanoimpurities of opposite sign, in the spirit of the ones in Ref. 24 (for differential-length nanoenhanced micropores), the so-called lubrication model of Refs. 25–27 (developed for electrophoresis applications), or other stochastic impurity-trapping models^{28–30}. We supplement these probabilities with continuity equations for the flow and number of trapped and free impurities. Then we integrate these formulae in time and space employing the capabilities of modern parallel computers, what allows us to track the nanofiltration process without a many-particle molecular dynamics simulation (which would be much more prohibitive due to the multi-scale nature of the system).

Our model calculates the evolution with position and time of the spatial profiles of the trapped-impurity layer in the pore inner walls, and the filtration figures of merit may be obtained from such evolution. Our results identify some pore geometries (*e.g.*, decreasing-conical and sinusoidal-corrugated) with about 4-fold larger initial nanofiltering performance and operational lifetime than simple cylinders of the same average diameter. The optimal geometry is also shown to depend on the LRV value acceptable for each specific application. Some general trends seem to emerge from our simulations, like the tendencies for impurities to accumulate faster when closer to the entry point of the flow and in the narrowest portions of the pores (these last two trends being either

competing or cooperating depending on the specific considered geometry). The observed effect cannot be explained alone by the mere consideration of whether the fluid is made to flow closer to the nanostructures - it is instead a consequence of the special stochastics of the process (for instance, increasing and decreasing cones have different filtration evolution in spite of exposing the same nanostructured area and having the same percent of fluid flowing near a given distance from the walls).

II. MODELS AND METHODS

In this Section, we detail our methods to evaluate the nanofiltration performance, the energy required for nanofiltration, and their evolution with time, for different micrometric-scale nominal geometries. A rapid overview is as follows: We build (Subsects. II A and II B) custom stochastic considerations that combine cumulative probabilities of electrostatic-type wall-impurity attraction, and of binding once impurities collide with the nanostructures in the walls, taking into account the evolution with space and time as flow passes and impurities progressively saturate the attractive and anchoring nanostructures in the wall. These stochastic considerations are then combined with continuity equations (Subsect. II C), resulting in a model that allows to track the nanofiltration. We then write the relationships and methods (Subsects. II D to II F) to derive from these results the relevant filtration properties such as logarithmic removal value LRV, operational lifetimes, energy balances, or spatial profiles of the trapped-impurity layer in the pore inner walls.

A. Initial considerations

Let us consider a tubular conduit of micrometric-scale diameter whose inner walls have a (initially homogeneous) nanotexture. The tube has a nominal diameter $d(x)$ that may, in general, vary along the axial coordinate x (with $0 \leq x \leq L$, where L is the tube length). A fluid passes through, carrying a certain concentration of nanoimpurities to be filtered out. All of the impurities are taken to be equal and have average radius ρ_0 . Let us try to obtain the evolution with space x and time t of the impurity concentration $C_{\text{imp}}(x, t)$ in the fluid and of the areal density of impurities $n(x, t)$ trapped in the tubes (throughout this article, by “areal density” we refer to quantities normalized using the nominal area of the tube inner wall).

Initially ($t = 0$) the system is in the “clean state”, in which $n(x, 0) = 0$ and the diameter available to the flow is $d(x)$. As time and flow passes, impurities get trapped and progressively cover the tube inner walls. Eventually, a “saturated state” is reached in which the nanotexture of the walls no longer electrostatically attracts further impurities. In the saturated state, n is n_{sat} and the diameter available to the flow decreases down to a value $d(x_i) - \delta_{\text{sat}}$. We will consider in this article that after this saturated state the capability of the walls to anchor further impurities is zero (and hence the filtration performance) so that we neglect conventional filtration mechanisms and focus only on the enhancement due to the nanotexture.

In order to evaluate the effects of variations of the diameter along the tube’s axial coordinate, and also to allow computation of successive spacial and temporal finite-difference iterations, we discretize the problem as follows: We divide the tube into $i = 0, 1, \dots, N$ parallel slices of coordinates $x_i = (L/N)i$ and also discretize time as $t_{j+1} = t_j + \Delta t_j$ with $j = 0, 1, \dots$ (the reason to allow the time step to vary with j will be to optimize our computational algorithms, see Sect. II E).

B. Stochastics

We will model the filtration process using the following stochastic description: We consider a collision rate with the pore walls for the impurities flowing in the fluid, and also a binding probability to the nanotexture once the impurity has collided with the wall, both quantities being time and space-dependent (*e.g.*, via the number of impurities that remain nonsaturated by trapped impurities at each given instant and position). Let us consider both contributions in that order:

As mentioned in the introduction, the good filtration rate of nanostructured micrometric pores cannot be explained if the only impurities colliding with the walls are those passing closer to them than a distance of the order of the size of the impurities. Instead, it is necessary to consider the effects of electrostatic attraction, that enlarges the escape distance below which the impurities will eventually collide with the nanotextured wall. We thus introduce a collision distance ρ_e as the typical impurity-wall separation below which an impurity in the flow will acquire course of collision with the wall. We expect ρ_e to grow with some form of effective charge of the walls (proportional to their ζ -potential) that will decay with time as impurities cover the wall and screen out the charges exposed in the nanotexturing. Using simple electrostatic escape distance arguments it may be expected that ρ_e should linearly grow with the effective charge of the walls. As shown,

e.g., in Ref. 24 (see also Ref. 23), a more precise law may be obtained when taking also into account the screening due to the Debye length of the fluid λ_D .^{23,24}

$$\rho_e(x_i, t_j) = \rho_0 + \lambda_D W \left(\frac{\rho_{e0} - \rho_0}{\lambda_D} \left(1 - \left\| \frac{n(x_i, t_j)}{n_{\text{sat}}} \right\| \right) \exp \left(\frac{\rho_{e0} - \rho_0}{\lambda_D} \right) \right), \quad (1)$$

where ρ_{e0} is the collision distance in the clean state, $W(x)$ is the the principal Lambert function and the notation $\|x\|$ stands for $\min(1, x)$.⁴³ Obtaining the ratio of impurities that travel within such collision distance ρ_e from the walls is now a classical hydrodynamic problem, for which we shall use the typical Poiseuille profile of velocity distributions for moderate external pressure-driven flows. This leads to the fraction f_e of impurities that will collide the the i -th slice of the walls:

$$f_e(x_i, t_j) = \left(\left(\left\| \frac{2\rho_e(x_i, t_j)}{d(x_i) - n(x_i, t_j)\delta_{\text{sat}}/n_{\text{sat}}} \right\| - 1 \right)^2 - 1 \right)^2. \quad (2)$$

In principle other more complicated velocity profile distributions could have been used but, as shown, *e.g.*, in Refs. 44 and 45, the flow may be in fact expected to be in the Poiseuille regime if the radiuses of the pores remain $\gtrsim 10$ nm and the values of viscosity and hydrostatic pressure are realistic for most filtering applications. (Note also that this is in contrast to the electrical-driven-like flow assumed in the models of Refs. 25–27 focused in electrophoresis scenarios). We are also implicitly assuming negligible turbulence and axial advection on the transversal dynamics (as valid for moderate flow velocities; see also Subsect. II F for a more comprehensive discussion of this latter aspect and the implications over the parameter values we shall choose for our numerical evaluations).

Concerning the impurity-wall binding probability for the impurities that do collide with the walls, it has to start from a maximum value Ω_0 in the initial clean state and then linearly decrease with the number of binding centers in the nanotextured walls, *i.e.*, with $n(x, t)$.

Both of the aforementioned probabilities have to be multiplicatively accumulated so to obtain the fraction of impurities being trapped in each finite-element slice of the tube, at any given time and with the walls screened out by a concentration of previously trapped impurities. This results in

$$f_{\text{trapped}}(x_i, t_j) = \frac{L}{N} f_e(x_i, t_j) \Omega'_0 \left(1 - \left\| \frac{n(x_i, t_i)}{n_{\text{sat}}} \right\| \right), \quad (3)$$

where

$$\Omega'_0 = (N/L)[1 - (1 - \rho_0\Omega_0)^{L/\rho_0N}] \quad (4)$$

is a correction to Ω_0 necessary when considering finite-element slices of length $\Delta x = L/N$.⁴⁶

C. Continuity equations and recursive finite-difference calculation of $n(x_i, t_j)$, $C_{\text{imp}}(x_i, t_j)$ and $\Phi(t_j)$

By using the aforementioned probabilities, finite-difference-iterative expressions may be now obtained for the areal density of trapped impurities $n(x_i, t_j)$ in each x_i slice of the tube at the time t_j , for a fluid flow rate $\Phi(t_j)$ passing through the tube carrying a concentration of impurities $C_{\text{imp}}(x_i, t_j)$. Specifically, the continuity condition for the impurity number gives for the areal density of trapped impurities:

$$n(x_i, t_{j+1}) = n(x_i, t_j) + \frac{\Delta t_j C_{\text{imp}}(x_i, t_j) \Phi(t_j) \Omega'_0}{\pi d(x_i)} \left(1 - \left\| \frac{n(x_i, t_j)}{n_{\text{sat}}} \right\| \right) f_e(x_i, t_j). \quad (5)$$

and for the concentration of impurities in the fluid arriving to the next Δx slice:

$$C_{\text{imp}}(x_{i+1}, t_j) = C_{\text{imp}}(x_i, t_j) - \frac{\pi L d(x_i)}{N \Delta t_j \Phi(t_j)} \left(n(x_i, t_j) - n(x_i, t_{j-1}) \right). \quad (6)$$

For the fluid flow rate $\Phi(t_j)$, as already mentioned above we will assume in this article that the liquid is driven by a constant hydrostatic pressure difference P between opposite ends of the tubular conduits. Thus, we use a Poiseuille relationship:^{24,25,44}

$$\Phi^{-1}(t_j) = \frac{128 \eta L}{\pi P N} \sum_i \left(d(x_i) - \frac{n(x_i, t_j) \delta_{\text{sat}}}{n_{\text{sat}}} \right)^{-4}. \quad (7)$$

Note that the flow rate becomes t -dependent even with constant P , due to the progressive narrowing of the pore as it becomes dirtier. Eventually, if $d(x_i) - n(x_i, t_j) \delta_{\text{sat}}/n_{\text{sat}} = 0$ at some x_i , the conduit would clog and $\Phi = 0$.

D. Figures of merit for filtration functionality: Logarithmic removal value LRV, operational lifetimes and energy consumption per trapped impurity

As customary,⁷⁻¹⁷ we will characterize the filtration performance through the so-called logarithmic removal value:

$$\text{LRV}(t) = -\log_{10} \frac{C_{\text{imp}}(x=L, t)}{C_{\text{imp}}(x=0, t)}. \quad (8)$$

For instance, 99.9% impurity removal corresponds to $\text{LRV}=3$. We will use the notation LRV_0 for $\text{LRV}(t=0)$, corresponding to the clean state of the filter. It is interesting to note that it is possible within our stochastic model to obtain explicit expressions for LRV_0 for each of the geometries

considered in this article. We describe them in an Appendix. We have checked that application of those direct equations provide the same results as the $t \rightarrow 0$ limit of our numerical finite-difference evaluations presented in Sect. III.

To characterize the endurance of the filter, let us introduce the $\text{LRV} \geq 5$, $\text{LRV} \geq 2$ and $\text{LRV} \geq 1$ lifetimes, defined as the t -values at which the LRV becomes 5-log, 2-log and 1-log, respectively. In practice, which of these endurance criteria (5-log to 1-log) is more relevant will depend on the specific application intended for the filter (*e.g.*, pathogen removal down to clinically safe levels vs. pre-filtration stage in industrial effluent treatments). Also, we will find useful to define the times at which certain thresholds are reached for the concentration of trapped impurities in the pore walls. So, we introduce the times $t_{0.15}$, $t_{1/2}$ and t_{sat} as those when the average areal density of trapped impurities in the whole tube, $\bar{n}(t)$, becomes respectively $0.15n_{\text{sat}}$, $0.5n_{\text{sat}}$ and n_{sat} .

One of the key advantages of nanostructured micrometric pore filters vs. alternatives such as size-exclusion nanopore membranes is their lower hydrodynamic resistance and correspondingly lower pressure required to achieve the fluid flow. Therefore, a quantity of importance is the energy consumed by the filtration, E , that can be evaluated by integrating in time the product of the flow rate and external pressure (*i.e.*, the hydrodynamic dissipated power).⁴⁷ Probably still more important is the energy normalized by the number of trapped impurities, henceforth noted as \mathcal{E} . It is not difficult to arrive to the following relationship linking the time evolutions of \mathcal{E} and LRV:

$$\mathcal{E}(t) = \frac{P}{C_0 (1 - 10^{-\text{LRV}(t)})}. \quad (9)$$

E. Computational procedures

The Eqs. (5) to (7) form a set that may be computationally integrated iteratively to obtain the x - and t -evolution of the pore filter. For that purpose, we implemented ad-hoc software that accepts arbitrary user-defined geometries for the nominal diameters $d(x)$. It iterates in both the j and i indexes (parallelizing the process so to use GPU accelerators), continuously calculating self-adaptively the time steps Δt_j by requiring that successive instants vary $n(x_i, t_j)$ less than 0.01% (for all x_i values). This results in about 10^4 time-intervals for each simulation. For the spacial discretization, we divided the tubular pores into $N = 10^6$ finite-difference slices (this leads in our simulations to a trapping probability for each impurity colliding with the walls always below 10^{-4} per finite-difference x -slice).

For the boundary conditions of our simulations we take as initial state $n(x,0) = 0$ (*i.e.*, clean state for $t = 0$) and $C_{\text{imp}}(x \neq 0,0) = 0$. For the spatial boundary condition we take $C_{\text{imp}}(0,t) = C_0$ (*i.e.*, a constant impurity concentration for the fluid at the entry of the pore).

F. Typical parameter values

For the various parameters describing the characteristics of the nanofunctionalized micrometric pore conduits in Eqs. (5) to (7) we use values of the same order of magnitude as the ones that were used in Ref. 24 to discuss (but not considering the effects of the pore micrometric geometry) available systems⁷⁻¹² with nanocoatings of varied compositions. We use nanoimpurity radius $\rho_0 = 10$ nm, effective collision distance in the clean state $\rho_{e0} = 30$ nm, binding probability in the clean state $\Omega_0 = 10^{-4}/\text{nm}$, saturation impurity layer thickness $\delta_{\text{sat}} = 40$ nm and saturation impurity areal density $n_{\text{sat}} = 10^{-2} \text{ nm}^2$. For the Debye length, we will use $\lambda_D = 10$ nm.

We also use an incoming impurity concentration $C_0 = 10^{10}/\text{m}^3$, the viscosity typical of water $\eta = 10^{-3}$ Pa s, and a pressure difference $P = 10^5$ Pa, values that are of the same order as the experimental conditions imposed in Refs. 7-12. But we have checked that the results of our simulations are invariant with respect to these last three parameters except for a multiplicative rescaling of the time values. This effect is due to the symmetry of the starting equations. Consequently, in the present article we shall preferentially express the times resulting from all our simulations normalized with respect to a common reference value t_{ref} . In particular, for this t_{ref} we will choose, for all the considered geometries (and as described in detail in Sect. III A), the half-saturation time $t_{1/2}$ of the cylindrical cylinder with diameter 300 nm. Increases in η would increase t_{ref} linearly, while increases in C_0 and P would induce an inversely proportional change in t_{ref} .

Concerning the size of the pores, we will always use a millimetric length $L = 1$ mm. For their diameter, in general we will use minimum, average and maximum values of, respectively, 200 nm, 300 nm and 400 nm. In the case of the diameter being constant (*i.e.*, cylinder pores) we will also check the effect of increasing it, scanning from 300 nm to 400 nm. (Note here that, with these pore dimensions, the area covered by anchoring centers, *i.e.*, the inner surface of the pore, is about four orders of magnitude larger than the transversal area; this alone explains already why the saturation capacity of a membrane of nanostructured micrometric pores is well larger than the one of a equivalently-sized membrane composed of nanometric pores filtering by transversal

size-exclusion effect.)

Finally, let us briefly comment at this point that the above typical parameter values (especially pressure) correspond to moderate flow velocities, in particular small enough for the assumption that axial advection effects do not complicate the recovery of the equilibrium in the transversal concentration profile of impurities as they are filtered out.²⁴ This is because the typical time it takes for diffusion to rebuild transversal equilibrium is orders of magnitude smaller than the typical time each impurity travels within the collision distance from the walls before being removed from the liquid: The first of those times may be estimated as λ^2/D ,⁴⁸ where D is the diffusion coefficient ($\sim 10^{-9}\text{m}^2\text{s}$) and λ the typical transversal distance over which equilibrium has to be reestablished (that may be taken somewhere between λ_D and ρ_e , *i.e.*, 10–30 nm). This leads to times of the order of 10^{-6} s. In contrast, the typical time that each impurity travels within the collision distance from the walls before being removed from the liquid may be estimated to be about 4×10^{-2} s (by combining an average Poiseuille velocity $Pd^2/(32L\eta)$, a typical diameter 300 nm and a typical distance traveled before being trapped $\Omega_0^{-1} = 10^{-5}$ m).

III. RESULTS AND DISCUSSION

A. Cylindrical conduits as a function of diameter

We first explore the filtration characteristics of cylinders as a function of their diameter. For that purpose, we computationally integrated our equations using for the diameter function $d(x)$ different constant values (the rest of the parameters being, for all the cylinders, equal to those detailed in Sect. II F). The Table I and the panels (a) to (d) of Fig. 1 display the results of our simulations for representative example diameters. In particular, the left-hand column (*i.e.*, panels (a) and (c)) shows the internal profile of the trapped-impurity layer in each tube at different instants of the time evolution, *i.e.*, their true internal radius as the conduits become narrower due to the accumulation of trapped impurities. These profiles are shown for the following instants of time: For $t = 0$ or clean state (when the radius coincides with its nominal value $d(x)/2$); for $t = t_{\text{sat}}$, *i.e.*, when all of the conduit has reached its saturated state (and the internal radius equals $(d(x) - \delta_{\text{sat}})/2$); and also for the two intermediate times $t_{0.15}$ and $t_{1/2}$ (when the average areal density of trapped impurities in the whole tube $\bar{n}(t)$ equals $0.15n_{\text{sat}}$ and $0.5n_{\text{sat}}$).

A first result of our simulations, already easily visible in the panels (a) and c of Fig. 1, is that the impurities accumulate first at the beginning of the cylinders, instead of uniformly.

The right-hand column of Fig. 1 shows the time-evolution of the areal density of trapped impurities at opposite ends of the cylindrical tube, $n(x = 0, t)$ and $n(x = L, t)$. It also shows the average areal density $\bar{n}(t)$ used to calculate the times $t_{0.15}$ and $t_{1/2}$ (that are marked as solid points in that curve). The timescale in this figure is normalized as t/t_{ref} , where t_{ref} is chosen as the $t_{1/2}$ value of the cylinder with diameter 300 nm; the same common t_{ref} will be used in all of the figures and tables of the present work.

These representations evidence that for cylindrical conduits the growth with time of $n(x, t)$ happens earlier when closer to the start of the tube ($x = 0$) than when closer to the exit point ($x = L$), by at least one order of magnitude in time value (note that the time axis is logarithmic). As it could be expected, the behavior of $\bar{n}(t)$ is intermediate between the ones at both edges of the conduit.

The results of our simulations also serve to study the influence of the diameter of the cylinders over the filtration performance and operational lifetimes given by the logarithmic removal value LRV. In Table I we list for each diameter the LRV value computed at the initial time, LRV_0 , that characterizes the maximum filtration capability of the cylinder (achieved in the initial, clean state). It may be noted that smaller diameters lead to better LRV_0 . The Table I also lists the times at which

TABLE I. Logarithmic removal value at the initial $t = 0$ clean state LRV_0 , and operational lifetimes for different LRV thresholds, for nanofunctionalized micrometric pores of different geometries and average diameters. The times are expressed normalized by the same common reference t_{ref} as in Figs. 1 and 2.

pore geometry & average diameter	LRV_0	$\text{LRV} \geq 5$ lifetime	$\text{LRV} \geq 2$ lifetime	$\text{LRV} \geq 1$ lifetime
cylinder 300 nm	5.6	$0.17 t_{\text{ref}}$	$1.28 t_{\text{ref}}$	$1.71 t_{\text{ref}}$
cylinder 350 nm	4.3	-	$0.77 t_{\text{ref}}$	$0.95 t_{\text{ref}}$
cylinder 400 nm	3.3	-	$0.39 t_{\text{ref}}$	$0.53 t_{\text{ref}}$
increasing cone 300 nm	6.2	$0.22 t_{\text{ref}}$	$1.79 t_{\text{ref}}$	$2.93 t_{\text{ref}}$
decreasing cone 300 nm	6.2	$0.76 t_{\text{ref}}$	$2.18 t_{\text{ref}}$	$2.53 t_{\text{ref}}$
sinusoid-corrugated 300 nm	6.4	$0.64 t_{\text{ref}}$	$2.66 t_{\text{ref}}$	$3.56 t_{\text{ref}}$

the LRV reaches the thresholds $\text{LRV}=5$, $\text{LRV}=2$ and $\text{LRV}=1$. Logically, the $\text{LRV} \geq 5$ lifetime is null for the cases in which $\text{LRV}_0 < 5$. Our results indicate that these lifetimes become significantly larger when the diameter becomes smaller, in line with the trend of LRV_0 . This also makes sense when comparing to each other the panels (b) and (d) of Fig. 1: this comparison evidences a similar type of change in the times at which the $n(t)$ curves reach the saturation value (and, in fact, $t_{0.15}$ and $t_{1/2}$).

The time evolution of the LRV performance is represented in further detail in Fig. 2 for the cylinder with 300 nm diameter.

The evolution of the energy \mathcal{E} consumed per trapped impurity as a function of the amount of impurities that got accumulated into the pore is represented in Fig. 3 for the cylinder with 300 nm diameter. It may be noticed that it only increases considerably past the $\text{LRV}=2$ lifetime (a result that in fact will hold for all the geometries studied in this work). The initial, clean-state value $\mathcal{E}(t=0)$ is almost the same (well within 0.1%) for all the studied cylinder diameters.

B. Cones of diameter increasing in the direction of flow.

Let us now show that other conduit geometries may improve the filtration performance and/or operational lifetimes with respect to those obtained for cylinders. We begin that investigation by studying conical tubular conduits with diameter increasing in the direction of the fluid flow. Note that these are indeed feasible micrometric geometries: there exist experimental realizations of membranes with conical (increasing and decreasing) pore shapes^{36–38} for different applications, such as the study of resistive-pulse biosensors³⁶ or capillary electrophoresis³⁸. However, to our knowledge there are not yet investigations of the nanofunctionalization of the inner surface of conical-shape pores for filtration applications.

In panels (e) and (f) of Fig. 1 we present the results obtained by performing our simulations with the $d(x)$ function corresponding to the increasing-conical geometry. In particular, the diameter increases linearly from the value 200 nm at the entrance to the tube up to the value 400 nm at the exit point (this is to be compared therefore with the 300 nm cylinder). Again it is visible that impurities accumulate sooner at the entrance of the tubes than at their exit. But it can be noticed in the figures that the differences are now even larger than in the cylindrical case. As a consequence, the $\bar{n}(t)$ evolution also spreads over a wider t -range.

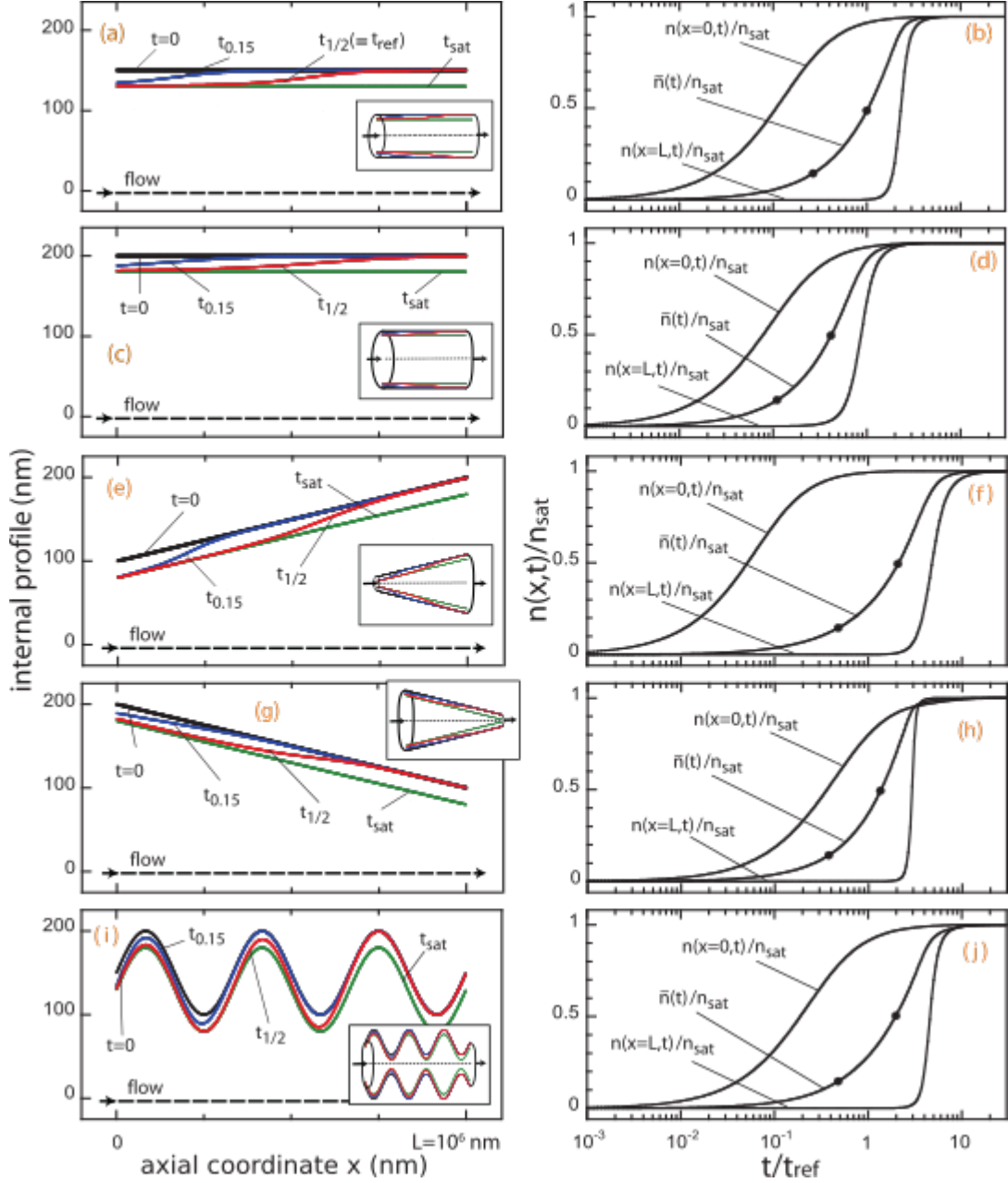


FIG. 1. Evolution of the layer of trapped impurities as flow passes through the nanostructured pores of the micrometric geometries indicated in the insets (cylinders of diameters 300 and 400 nm, increasing and decreasing cones, and sinusoidal corrugations). Left column: spatial profiles of the adsorbed layer, for selected times. Right column: time evolution of the areal density n of trapped impurities, for the entry and exit points and for the spatial average \bar{n} . The times $t_{0.15}$ and $t_{1/2}$ are defined by $\bar{n} = 0.15n_{\text{sat}}$ and $0.5n_{\text{sat}}$ (marked as solid points in the second column) and t_{sat} corresponds to saturation ($\bar{n} = n_{\text{sat}}$). The time axis is normalized by a common t_{ref} defined as $t_{1/2}$ of the 300 nm cylinder. Note the (sometimes competing) tendencies of accumulation being faster both near the entry of the pore and in its narrowest points.

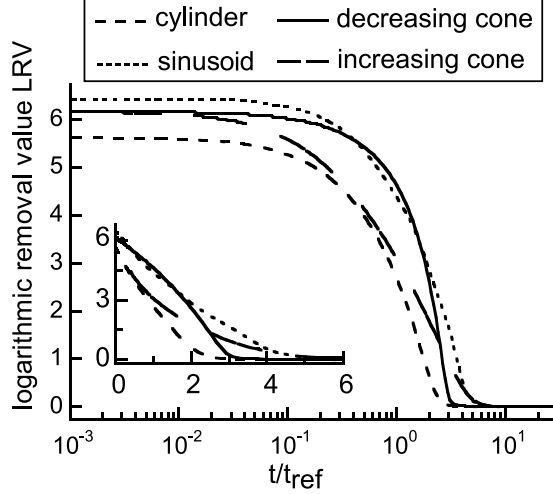


FIG. 2. Logarithmic removal value LRV as a function of time obtained for nanofunctionalized micrometric pores with different geometries and average nominal diameter 300 nm. Note that the cylinder leads to the lowest initial value, LRV_0 , and lowest operational lifetimes (see also Table I). The time axis is normalized by the same common reference t_{ref} as in Figs. 1 and Table I.

As it may be noticed from the values listed in Table I, the initial filtration performance LRV_0 achieved by the increasing cone improves the one of the equivalent 300 nm cylinder (6.2-log versus 5.6-log, or about 4 times smaller concentration of impurities in the fluid at the exit of the pore).

The Table I also indicates that the increasing-cone geometry produces operating lifetimes larger by about 30% (for the $LRV \geq 5$ criterion), 40% (for the $LRV \geq 2$ criterion) or 70% (for the $LRV \geq 1$ criterion) with respect to cylinders with the same average diameter. These differences are also illustrated in Fig. 3, that compares the $LRV(t)$ curves of conduits with different shapes (but with equal average diameter 300 nm). We note again that the time axis in all our figures is expressed normalized by a common reference value (t_{ref} defined as $t_{1/2}$ of the $d = 300$ nm cylinder) and in logarithmic scale.

These results indicate, therefore, that a possible path to greatly increase the operational lifetime of nanoenhanced pore filters is to employ supporting micrometric geometries with variable diameter. In the following Sections this conclusion will be confirmed with other pore shapes.

In relation to the energy consumption per filtered impurity, Fig. 2 shows that (as already found for cylinders) it only increases appreciably as time passes the $LRV=2$ lifetime. Also the initial value of \mathcal{E} is similar to the cylinder with the same average diameter (would be indistinguishable in the horizontal axis range of Fig. 2, as in fact will happen for all geometries studied in this

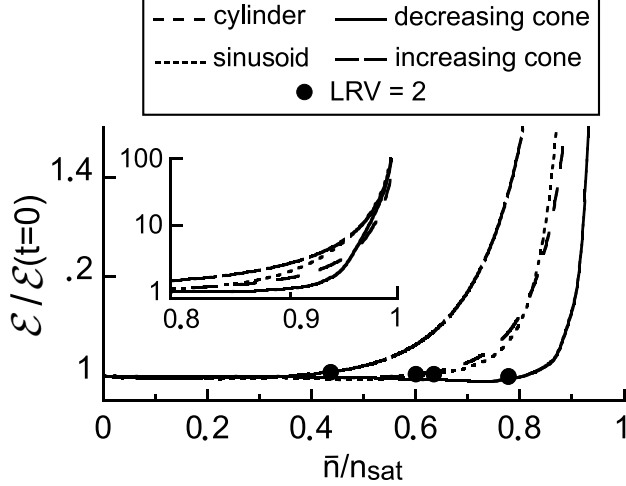


FIG. 3. Energy per filtered impurity obtained for nanofunctionalized micrometric pores with different geometries and average nominal diameter 300 nm, normalized to its initial value in the same pore (or in the reference 300 nm cylinder; the difference would be unobservable in the figure). Note the increase after the LRV=2 threshold (solid dots), that in turn is reached (see Table I) at quite different times for each geometry.

work; for that reason the figure just expresses \mathcal{E} normalized to its initial value). Therefore, the main difference with respect to the equivalent cylinder is that such LRV=2 threshold is reached, as mentioned before, about 40% later in time.

C. Cones of diameter decreasing in the direction of flow.

We consider now a decreasing-conical geometry, *i.e.*, a linearly decreasing diameter $d(x)$ function. Again we use in our simulations 200 and 400 nm for the extreme diameter values, and the mean diameter along the axial direction remains 300 nm. Panels (g) and (h) of Fig. 1 illustrate the results of our simulations for that geometry. A significant qualitative difference with respect to the previous increasing-cone conduit is that now the plots versus time of $n(x=0,t)$ and $n(x=L,t)$ are significantly closer to each other. In fact, near the saturation state both lines even cross each other. This means that no longer is always true that the beginning of the conduit, $x=0$, accumulates impurities faster than its end, $x=L$. Instead, the smaller section at the end of the cone is able to overcome the rhythm of impurity accumulation of the first slices of the cone before these get saturated.

This more uniform filling by impurities results in a different evolution with time of the filtration

performance. As revealed by the values listed in Table I (see also Fig. 3), the initial LRV values of the increasing and decreasing cones are coincident, but the $\text{LRV} \geq 5$ lifetime of the decreasing cone is even longer than the one of the increasing cone (about 3.5 times longer than in the increasing cone, and about 4.5 times longer than in the cylinder of equal mean diameter). In contrast, the $\text{LRV} \geq 1$ lifetime of decreasing cones is shorter than the one of increasing cones (about 15% shorter, though still about 50% longer than for equivalent cylinders). On the other hand, the $\text{LRV} \geq 2$ criterion reveals an intermediate tendency, getting a higher lifetime in comparison both with the cylinder (70% higher) and the increasing-cone (20% higher). This can be understood by observing in Fig. 3 that the $\text{LRV}(t)$ curves of both types of conical shapes cross each other near $\text{LRV} \sim 1.5$.

In relation to the energy consumed per impurity filtered out, this geometry follows some trends similar as cylinders and increasing cones: The initial value is similar to those geometries and again (see Fig. 2) it almost does not increase with time until the $\text{LRV}=2$ point. However, it also presents some differences in that such $\text{LRV}=2$ point happens at considerably larger \bar{n}/n_{sat} and that beyond this point decreasing cones actually degrade faster than cylinders and increasing cones.

D. Sinusoid-corrugated tubular conduits.

Let us now consider corrugated tubular-like pores, of diameter increasing and decreasing successively along their axis. Again this micrometric pore geometry is experimentally realizable and studies do exist on networks composed by (non-nanostructured) micrometric pores with spherical shape and interconnections (throats) of small radius forming sinus-like geometries.³⁵ Also, some theoretical studies have analyzed porous systems as a network of pores with sinus-like shapes.^{39,40}

A $\sin(x)$ -like diameter functionality is possibly one of the simplest of the corrugated geometries, and could a priori be expected to serve as a fair first approximation to, at least, the most essential features of real corrugated pores.^{35,39,40} In panels (i) and (j) of Fig. 1 we present the results for our simulations using for the diameter profile the function $d(x) = (300\text{nm}) + (100\text{nm})\sin(6\pi x/L)$, *i.e.*, the maximum, minimum and mean diameter are the same as in the previous two Subsections, and $d(x)$ presents three oscillations over the conduit's length (we have checked that increasing the number of oscillations would not qualitatively affect our results; note also that according to Eq. (A.5) $\text{LRV}_0^{\text{sinus}}$ does not depend on the number of oscillations).

The time-evolution of the internal profiles shown in panel (i) of Fig. 1 evidences that in the

corrugated conduits the impurities accumulate first in the initial oscillation periods, and within that tendency they accumulate first in their narrower portions. This result is coherent with a naïve vision of crudely considering the corrugated conduits as a combination in series of alternately increasing and decreasing cones. The time-evolution of the average $\bar{n}(t)$ and of the filtration performance $\text{LRV}(t)$ also resembles somewhat the results obtained for cones. However, it must be noted that the initial LRV performance is better than the one of the cylindrical and conical shapes (see Table I and Fig. 3). The difference is almost of one logarithmic unit with respect to the cylinder. Concerning the operational lifetime, with the $\text{LRV} \geq 5$ criterion it is almost as long as in the decreasing cone (16% shorter) and still much longer than for cylinders (almost 4 times longer). This is achieved without penalizing the $\text{LRV} \geq 1$ lifetime: on the contrary, with the $\text{LRV} \geq 1$ criterion the operational lifetime is even longer (about 20%) than for decreasing cones. The $\text{LRV} \geq 2$ lifetime is also favorable (about double than for 300 nm cylinders).

In terms of the hydrodynamic energy rate, it can be seen in Fig. 2 that for $\bar{n}/n_{\text{sat}} < 0.9$ the sinusoid geometry mimics quite well the behavior of its equivalent cylinder. However, for higher values, the sinusoid becomes energetically less efficient, and starts to become more similar to the increasing cone, which is the one less efficient. Of course, other difference with the cylinder is that the $\text{LRV}=2$ mark is reached at significantly later time, as already mentioned.

IV. CONCLUSIONS

To sum up, we have studied the nanofiltration achieved by individual pores of micrometric diameter with nanostructured inner walls, as a function of the micrometric-scale geometry. We focused on their logarithmic retention value LRV in the initial or clean state, on its evolution with time, on their operational lifetime for different acceptable LRV thresholds, on the energy consumed by the filtration, and on the evolution of the inner radius of the pores as impurities accumulate over their walls. For our studies, we wrote stochastic equations taking into account the special attraction effect of the nanotextured surfaces due to their electropositivity (or negativity) and also the necessary continuity equations for the flow and trapping of nanoimpurities. We considered different geometries, including first cylinders of different diameters and then pores with diameter varying along the direction of the fluid flow (increasing and decreasing conical tubes and sinusoid-corrugated tubes).

Our results indicate that, in spite of the large mismatch between the nano- and micro-scales of these systems, the nanofiltration performance and its time-evolution do depend also on the micrometric geometry.

With regard to the diameter size for cylindrical micrometric pores, we found that decreasing it improves LRV_0 (and this enlarges the operational times during which the LRV is above a threshold.)

Concerning pores with micrometric diameter varying along the flow direction, we found that these variations allow to improve the filtration characteristics without decreasing the average diameter of the conduit. In particular *i*) increasing-conical conduits have, with respect to cylinders with the same average diameter, better initial LRV and significantly longer operational times (about 30-70% longer, depending on the acceptable LRV threshold); *ii*) decreasing-conical conduits equally improve the initial LRV and extend even further the operational times for high-LRV filtration requirements (more than 4.5 times longer than equivalent cylinders) while the low-LRV operational lifetime increases but to a lesser extent; and *iii*) sinus-corrugated tubular conduits improve the initial LRV values by almost one logarithmic unit with respect to equivalent cylinders, and extend the operational lifetimes for both high- and low-LRV requirements (almost 4 times and about 2 times longer than equivalent cylinders, respectively). All these geometries also extend, with respect to cylinders of equal average diameter, the period of time in which energy consumption per trapped impurity is favorable.

Our results also reveal two general tendencies in the process of impurity accumulation in the walls, that may be synergic or antagonist with each other depending on the specific geometry considered: The first trend is that the nanoenhanced walls get covered by nanoimpurities at a faster pace in the regions with smaller diameters; the second is that they get covered faster when nearer to the entrance of the flow in the pore. When both types of regions do not coincide in space, their competition may significantly increase some operational lifetimes. For example, when comparing increasing and decreasing conical pores, in spite of having equal initial LRV, their time evolution is significantly different from each other (note, *e.g.*, their $LRV \geq 5$ lifetimes in Table I).

Therefore, our results indicate that engineering of the micrometric geometry of pores (as in fact, experimentally achieved by several groups with pore shapes similar to the ones studied in this work³⁴⁻³⁸) should be applied to nanostructured micrometric pore filters to optimize their nanofiltration characteristics. This is specially so in the case of membrane filters, where our results should

be directly applicable (whereas for 3D media it may be expected that the specific tortuosity and flow locality of each given material and morphology should be additionally taken into consideration).

ACKNOWLEDGMENTS

We acknowledge support by University of Santiago de Compostela, Project 2024-PU036 ‘Propiedades de materiais supercondutores micro e nanoestruturados’.

AUTHOR CONTRIBUTIONS

J.C. Verde: Conceptualization (equal); Formal analysis (equal); Methodology (equal); Software (equal); Visualization (equal); Writing – original draft (equal). *N. Cotón*: Conceptualization (equal); Formal analysis (equal); Methodology (equal); Software (equal); Visualization (equal); Writing – original draft (equal). *M.V. Ramallo*: Conceptualization (lead); Formal analysis (equal); Methodology (equal); Software (equal); Visualization (equal); Writing – original draft (equal); Writing – review & editing (lead).

Appendix: Analytical expressions for LRV₀

Explicit analytical expressions for LRV₀ can be calculated for each of the geometries studied in Sect. II. For that, multiply over all x -positions the survival no-trapping probabilities to first obtain:

$$\text{LRV}(t) = - \sum_i \log_{10} \left[1 - \Omega'_0 \left(1 - \left\| \frac{n(x_i, t_j)}{n_{\text{sat}}} \right\| \right) \left[\left(\left\| \frac{2\rho_e(x_i, t_j)}{d(x_i) - n(x_i, t_j) \delta_{\text{sat}}/n_{\text{sat}}} \right\| - 1 \right)^2 - 1 \right] \Delta x \right]. \quad (\text{A.1})$$

For the initial, clean state ($t = 0$, $n(x_i, 0) = 0$ and $\rho_e(x_i, 0) = \rho_{e0}$) this reduces to:

$$\text{LRV}_0 = (\ln 10)^{-1} \int_{x=0}^L \Omega_0 \left[\left(\left\| \frac{2\rho_{e0}}{d(x)} \right\| - 1 \right)^2 - 1 \right]^2 dx, \quad (\text{A.2})$$

where we also recovered the continuous model by using $\Delta x \rightarrow dx$ and the power expansion $\log_{10}(1 - ydx) \approx -ydx/\ln 10$. Let us now carry out his integration for each given geometry.

For cylindrical pores of diameter $d = \rho_{e0} \delta$ (the ρ_{e0} normalization achieves compactness here):

$$\text{LRV}_0^{\text{cylinder}} = \frac{16\Omega_0 L}{\ln 10} \left[\frac{1}{\delta^2} - \frac{2}{\delta^3} + \frac{1}{\delta^4} \right]. \quad (\text{A.3})$$

We assumed $d > 2\rho_{e0}$; for the general case just replace $2/\delta$ by $\|2/\delta\|$.

For cones with maximum and minimum diameters $\rho_{e0} \delta_M$ and $\rho_{e0} \delta_m$:

$$\text{LRV}_0^{\text{cone}} = \frac{16\Omega_0 L}{3 \ln 10} \left[\frac{3}{\delta_m \delta_M} - \frac{\delta_m + \delta_M}{(\delta_m \delta_M)^2} + \frac{(\delta_m + \delta_M)^2 - \delta_m \delta_M}{(\delta_m \delta_M)^3} \right]. \quad (\text{A.4})$$

Again we assumed $d(x) > 2\rho_{e0}$ for notational simplicity. This result is valid both for increasing or decreasing cones, but note that they will have different time-evolution after their equal initial filtration performance, see Sects. III B and III C.

For a sinusoidally corrugated tube of maximum and minimum diameters $\rho_{e0} \delta_M$ and $\rho_{e0} \delta_m$ with an integer number n of oscillation periods:

$$\text{LRV}_0^{\text{sinus}} = \frac{\Omega_0 L}{\ln 10} \left[\frac{8(\delta_M + \delta_m)}{(\delta_M \delta_m)^{3/2}} + \frac{4(3\delta_M^2 + 2\delta_M \delta_m + 3\delta_m^2)}{(\delta_M \delta_m)^{5/2}} + \frac{(\delta_M + \delta_m)(5\delta_M^2 - 2\delta_M \delta_m + 5\delta_m^2)}{(\delta_M \delta_m)^{7/2}} \right]. \quad (\text{A.5})$$

Again we assumed $d(x) > 2\rho_{e0}$. The result is independent on n , as far as it is integer and nonzero.

The LRV(t) in Fig. 3 (and Table I) were obtained by numerical integration of Eqs. (5) to (7). Their limit values for $t \rightarrow 0$ fully coincide with the results of Eqs. (A.3) to (A.5).

REFERENCES

- ¹Darling, S.B. “Perspective: Interfacial materials at the interface of energy and water”. *J. Appl. Phys.* **124**, 030901 (2018).
- ²Sadik, O.A.; Du, N.; Yazgan, I.; Okello, V.; “Nanostructured Membranes for Water Purification”. In “Nanotechnology Applications for Clean Water”, 2nd Edition, p. 95. William Andrew Publishing: Norwich, USA (2014).
- ³Gehrke I.; Geiser A.; Somborn-Schulz A. “Innovations in nanotechnology for water treatment”. *Nanotechnology, Science and Applications* **8**, 1 (2015).
- ⁴Prakash, S.; Lin, G “Multiphysics of microfluidics and nanofluidics”. *J. Appl. Phys.* **133**, 120401 (2023).
- ⁵Jingwei Wu, J.; Pourdeyhimi, B.; Yarin, A.L. “Adaptable intelligent filters based on nanotextured nonwoven membranes containing water-insoluble hydrogels”. *J. Appl. Phys.* **135**, 084901 (2024).
- ⁶Theron, J.; Walker, J.A.; Cloete, T.E. “Nanotechnology and water treatment: applications and emerging opportunities”. *Crit. Rev. Microbiol.* **34**, 43 (2008).
- ⁷Wegmann, M.; Michen, B.; Graule, T. “Nanostructured surface modification of microporous ceramics for efficient virus filtration”. *J. Eur. Ceram. Soc.* **28**, 1603 (2008).
- ⁸Wegmann, M.; Michen, B.; Luxbacher, T.; Fritsch, J.; Graule, T. “Modification of ceramic microfilters with colloidal zirconia to promote the adsorption of viruses from water”. *Water Res.* **42**, 1726 (2008).
- ⁹Frank, H.; Lancaster, R.; “Electropositive Filtration Technology in Automobile Manufacturing Applications”. In the Proceedings of WQA-Aquatech 2008 Meeting, Mandalay Bay, Las Vegas, Nevada.
- ¹⁰Tepper, F.; Kaledin, L.; Kaledin, T. “Non-woven electrostatic media for chromatographic separation of biological particles”. *J. Liq. Chromatogr. R. T.* **32**, 607 (2009).
- ¹¹Tepper, F.; Kaledin, L. “Nanostructured chem-bio non-woven filter”. *Nanoscience and Nanotechnology for Chemical and Biological Defense* **1016**, 273 (2009).
- ¹²Ikner, L.A.; Soto-Beltran, M.; Bright K.R. “New method using a positively charged microporous filter and ultrafiltration for concentration of viruses from tap water”. *Appl. Environ. Microbiol.* **77**, 3500 (2011).
- ¹³Ly, Y.; Wang, Z.; Liu, S.; Hao, L.; Sang, Y.; Liu, D.; Wang, J.; Boughton, R.I. “Silver

- nanoparticle-decorated porous ceramic composite for water treatment”. *J. Membrane Sci.* **331**, 50 (2009).
- ¹⁴Hambusch, B.; Bösk, M.; Eberhagen, I.; Müller, U. “Removal of bacteriophages with different surface charges by diverse ceramic membrane materials in pilot spiking tests”. *Water Sci. and Technol.* **66**, 151 (2012).
- ¹⁵Meder, F.; Wehling, J.; Fink, A.; Piel, B.; Ki, K.; Frank, K.; Rosenauer, A.; Treccani, L.; Koepen, S.; Dotzauer, A.; Rezwani, K. “The role of surface functionalization of colloidal alumina particles on their controlled interactions with viruses”. *Biomaterials* **34**, 4203 (2013).
- ¹⁶Yang, D.; Fan, T.; Zhang, D.; Zhu, J.; Wang, Y.; Du, B.; Yan, Y. “Biotemplated hierarchical porous material: the positively charged leaf”. *Chem-Eur. J.* **19**, 4742 (2013).
- ¹⁷Yang, D.; Du, B.; Yan, Y.; Li, H.; Zhang, D.; Fan, T. “Rice-husk-templated hierarchical porous TiO₂/SiO₂ for enhanced bacterial removal”. *ACS Appl. Mater. Inter.* **6**, 2377 (2014).
- ¹⁸Zegeye, T.A.; Kuo, C.-F. J.; Wotango, A.S.; Pan, C.-J.; Chen, H.-M.; Haregewoin, A.M.; Cheng, J.-H.; Su, W.-N.; Hwang, B.-J. “Hybrid nanostructured microporous carbon-mesoporous carbon doped titanium dioxide/sulfur composite positive electrode materials for rechargeable lithium-sulfur batteries”. *Journal of Power Sources*, **324**, 239 (2016).
- ¹⁹Lu, T.; Cui, J.; Qu, Q.; Wang, Y.; Zhang, J.; Xiong, R.; Ma, W.; Huang, C. “Multistructured Electrospun Nanofibers for Air Filtration: A Review”. *ACS Appl Mater Interfaces* **13**, 23293 (2021).
- ²⁰Wu, M.-B.; Ye, H.; Zhu, Z.-Y.; Chen, G.-T.; Ma, L.-L.; Liu, S.-C.; Liu, L.; Yao, J.; Xu, Z.-K. “Positively-charged nanofiltration membranes constructed via gas/liquid interfacial polymerization for Mg²⁺/Li⁺ separation”. *Journal of Membrane Science* **644**, 119942 (2022).
- ²¹Deng, Y.; Lu, T.; Zhang, X.; Zeng, Z.; Tao, R.; Qu, Q.; Zhang, Y.; Zhu, M.; Xiong, R.; Huang, C. “Multi-hierarchical nanofiber membrane with typical curved-ribbon structure fabricated by green electrospinning for efficient, breathable and sustainable air filtration”. *Journal of Membrane Science* **660**, 120857 (2022).
- ²²Nassrullah, H.; Aburabie, J.; Hilal, N.; Hashaikeh, R. “Electroactive nanofiltration membranes based on carbon nanostructures for enhanced desalination performance”. *Journal of Water Process Engineering* **56**, 104405 (2023).
- ²³Walker, D.A.; Kowalczyk, B.; Olvera de la Cruz, M.; Grzybowski, B.A. “Electrostatics at the nanoscale”. *Nanoscale*, **3**, 1316 (2011).
- ²⁴Ramallo, M.V. “An effective-charge model for the trapping of impurities of fluids in channels

- with nanostructured walls”. *Nanoscale Res. Lett.* **8**, 19 (2013).
- ²⁵Ghosal, S. “Lubrication theory for electro-osmotic flow in a microfluidic channel of slowly varying cross-section and wall charge”. *J. Fluid Mech.* **459**, 103 (2002).
- ²⁶Ghosal, S. “The effect of wall interactions in capillary-zone electrophoresis”. *J. Fluid Mech.* **491**, 285 (2003).
- ²⁷Ghosal, S. “Fluid mechanics of electroosmotic flow and its effect on band broadening in capillary electrophoresis”. *J. Fluid Mech.* **25**, 214 (2004).
- ²⁸Krupp, A.U.; Griffiths, I. M.; Please, C.P. “Stochastic modelling of membrane filtration”. *Proceedings of the Royal Society A* **473**, 20160948 (2017).
- ²⁹ten Bosch, A. “Modeling transport and filtration of nanoparticle suspensions in porous media”. *Phys. Rev. E* **107**, 034121 (2023).
- ³⁰Tartakovsky, A.M.; Tartakovsky, D.M.; Meakin P. “Stochastic Langevin Model for Flow and Transport in Porous Media”. *Phys. Rev. Lett.* **101**, 044502 (2008).
- ³¹Miele, F.; de Anna, P.; Dentz, M. “Stochastic model for filtration by porous materials”. *Phys. Rev. Fluids* **4**, 094101 (2019).
- ³²Simeski, F.; Boelens, A.M.P.; Ihme, M. “Modeling Adsorption in Silica Pores via Minkowski Functionals and Molecular Electrostatic Moments”. *Energies* **13**, 5976 (2020).
- ³³Bizmark, N.; Schneider, J.; Priestley, R.D.; Datta, S.S. “Multiscale dynamics of colloidal deposition and erosion in porous media”. *Sci. Adv.* **6**, eabc2530 (2020).
- ³⁴Xu, Y.; Zhang, B. “Recent advances in porous Pt-based nanostructures: synthesis and electrochemical applications”. *Chem. Soc. Rev.* **43**, 2439 (2014).
- ³⁵Mehdizadeh, H.; Somo, S.I.; Bayrak, E.S.; Brey, E.M.; Cinar, A. “Design of Polymer Scaffolds for Tissue Engineering Applications”. *Ind. Eng. Chem. Res.* **54**, 2317 (2015).
- ³⁶Wharton, J.E.; Jin, P.; Sexton, L.T.; Horne, L.P.; Sherrill, S.A.; Mino, W.K.; Martin, C.R. “A Method for Reproducibly Preparing Synthetic Nanopores for Resistive-Pulse Biosensors”. *Small* **8**, 1424 (2007).
- ³⁷Apel, P.Y.; Korchev, Y.E.; Siwy, Z.; Spohr, R.; Yoshida, M. “Diode-like single-ion track membrane prepared by electro-stopping”. *Nucl. Instr. and Meth. in Phys. Res. B* **184**, 337 (2001).
- ³⁸Wu, X.; Rajaeskaran, R.; Martin, C. R. “An Alternating Current Electroosmotic Pump Based on Conical Nanopore Membranes”. *ACS Nano* **10**, 4637 (2016).
- ³⁹Balhoff, M.T.; Wheeler, M.F. “A predictive Pore-Scale Model for Non-Darcy Flow in Porous Media”. *SPE Journal* **14**, 579 (2009).

- ⁴⁰Veyskarami, M.; Hassani, A.H.; Ghazanfari, M.H. “Modeling of non-Darcy flow through anisotropic porous media: Role of pore space profiles”. *Chem. Eng. Sci.* **151**, 93 (2016).
- ⁴¹Thauvin, F.; Mohanty, K.K. “Network Modeling of Non-Darcy Flow Through Porous Media”. *Transport Porous Med.* **31**, 19 (1998).
- ⁴²Wang, X.; Thauvin, F.; Mohanty, K.K. “Non-Darcy flow through anisotropic porous media”. *Chem. Eng. Sci.* **54**, 1859 (1999).
- ⁴³We use the notation $\|x\|$ as a way to simplify our notation yet keeping our equations valid if the filter is beyond its saturation point. As the numerical evaluations in this article are relevant only until that saturation point, for most practical purposes $\|x\| = x$ in our present context.
- ⁴⁴Sparreboom, W.; van der Berg, A.; Eijkel, J.C.T. “Transport in nanofluidic systems: a review of theory and applications”. *New J. of Phys.* **12**, 015004 (2010).
- ⁴⁵Zhang, J.; Todd, B.D.; Travis, K.P. “Viscosity of confined inhomogeneous nonequilibrium fluids”. *J. Chem. Phys.* **121**, 10778 (2004).
- ⁴⁶This is because the survival (*i.e.*, non-binding) probabilities per unit length must accumulate multiplicatively (and not linearly) over successive differential lengths when considering a finite-length slice $(x_j, x_j + \Delta x)$. If we identify the minimum length over which Ω_0 makes sense with an impurity size ρ_0 , that condition translates to $(1 - \rho_0\Omega_0)^{\Delta x/\rho_0} = 1 - \Omega'_0\Delta x$ and hence to Eq. (4).
- ⁴⁷It could be thought that the hydrodynamic energy could be not the only one playing a role in this kind of filtration, and that the binding energy per impurity should perhaps be also considered. However, the latter becomes negligible in our case, as may be seen by an order of magnitude comparison: The more energetic bond between impurities and walls would be an ionic one, of typically 10^{-18} J per impurity. This is to be compared to Eq. (9) or about 10^{-5} J. Therefore, for the situation studied in this article the total energy required for filtration may be identified with the hydrodynamic rate.
- ⁴⁸E. L. Cussler; “Typical values of diffusion coefficients”. In “Diffusion Mass Transfer in Fluid Systems”, p. 143. Cambridge University Press: New York, USA (2007).